

## Estimating the Effects of Part Size on Direct Laser Deposition Parameter Selection via a Thermal Resistance Network Approach

Garrett J. Marshall<sup>1</sup>, Scott M. Thompson<sup>2, †</sup>, Steve R. Daniewicz<sup>3</sup>, Nima Shamsaei<sup>2</sup>

<sup>1</sup>Center for Advanced Vehicular Systems (CAVS), Mississippi State University, MS, 39762

<sup>2</sup>Department of Mechanical Engineering, Auburn University, Auburn, AL, 36849

<sup>3</sup>Department of Mechanical Engineering, University of Alabama, Tuscaloosa, AL, 35487

† Corresponding author:

Email: [scott.thompson@auburn.edu](mailto:scott.thompson@auburn.edu)

Phone: (334) 844-4820

### Abstract

A mathematical model for heat transfer during the Directed Energy Deposition (DED) process is proposed. The model employs the thermal resistance network analogy and is developed to aid one in predicting part size effects on its temperature distribution during manufacture, and in how to compensate such effects via suitable process parameter selection. The model predicts a pseudo steady-state temperature response in the melt pool. The temperature variation along the heat affected zone of a thin-walled part is estimated while assuming deposition is occurring far from the substrate. Predicted melt pool and bulk part temperatures are validated against Laser Engineering Net Shaping (LENS™) experimental data obtained via a dual-wavelength pyrometer and in-chamber infrared camera, respectively. Results demonstrate that the model may be used to predict an average melt pool temperature. Bulk, calculated temperature distribution needs to be further investigated to find a more suitable heat transfer coefficient surrounding the part.

### Introduction

Laser Engineered Net Shaping (LENS™) is a blown-powder, laser-based Directed Energy Deposition (DED) additive manufacturing (AM) process for metals fabrication originating from Sandia National Laboratories [1], [2]. In this process, a laser creates a molten pool as a CNC-guided substrate moves at a predefined speed and path, while metal powder is continuously injected into the pool to form a solid deposit/track. A part is thus fabricated track by track, and then layer by layer, in free space instead of within a powder bed. Due to the nature of its process, LENS offers the ability to control microstructure [3]–[5], fabricate parts of higher strength [6]–[9], and create functionally graded parts [10], [11]. The challenge still exists, however, to adequately understand and model thermal aspects of the process in order to best select the appropriate process parameters and to more confidently qualify fabricated parts for use in the field. The process-property-performance relationships inherent to LENS and its produced materials require one to relate process parameters to part thermal response during manufacture; allowing one to predict final microstructure and residual stress.

To determine the thermal response of LENS materials during manufacture, one may resort to numerical simulation or analytical modeling to solve the heat equation representing heat transfer in successive layers. In addition to thermal exchange with surroundings (including laser and chamber gas/walls) via radiation and convection, melt pool formation and solidification, as well as its fluid motion, can also be considered at varying levels of fidelity. Analytical solutions are desirable in that they offer an elegant representation of the thermal phenomena, e.g. cooling rates and temperature gradients, inherent to the process. Perhaps the most well-known of these is Rosenthal's solution to the 3D heat equation for a moving point heat source [12]. Originally intended for welding, the solution has since been applied to DED due to process similarities and has since aided the understanding of melt pool geometry and solidified microstructure for various AM process parameters [3], [13], [14]. Neither latent heat of fusion effects nor temperature-dependent properties are taken into consideration through Rosenthal's approach; and several researchers have noted the need for such information to be integrated for obtaining more accurate solutions [13], [15], [16].

Applying welding models to the DED process has challenges. These models tend to not include mass addition to the melt pool or the laser attenuation created by the DED powder flow. Welding may also deviate from the DED process when deposited surface is considered. For instance, many welded surfaces are large enough that the deposition plane may be considered infinite. In DED, however, a track could be deposited on such a plane where edge effects may need to be considered. A more recent solution to the DED process was sought by Gockel et al. [17] to describe these edge effects. They solved the heat equation for edge effects on a thin wall using the superposition of two point heat sources symmetric about the edge of the wall. Though thermal properties were temperature-independent, the solution to the melt pool geometry trended well with an FEA solution with temperature-dependent properties. Others have also formulated analytical models for various phenomena in DED such as clad geometry, beam attenuation, and powder heating that may be paired with other models for increased accuracy of results [18], [19].

Process maps (i.e. surface plots) have been developed from Rosenthal's solution for aiding process parameter selection [13], [14]. Process maps, in particular, show great potential in guiding the process parameter selection by describing melt pool and temperature response with a change in dimensionless operating parameters. The mapping scheme is realized by solving Rosenthal's equation with changing variables and using the temperature solution to determine thermal gradients and cooling rates. These values are then used to study effects on melt pool geometry, residual stress, and solidification microstructure. However, it can be difficult to incorporate different part geometries into Rosenthal-based maps since such solutions are based on parts with semi-infinite domains and no edge effects. A 'scaling factor' between geometries is desired.

This current study focuses on establishing and examining an alternate approach for predicting DED process and material property/size effects on subsequent thermal response. A purely-analytical thermal resistance network modeling approach is adopted herein. Via Ohm's analogy, the complex heat transfer occurring during DLD can be approximated as electrical current with one-dimensional flow along a nodal circuit containing various capacitors and resistors. Using such an approach allows one to isolate each mode and avenue for heat transfer and allows for a more intuitive representation of the thermophysics. The method is a 'piecewise', low-fidelity analytical approach enabling the determination of various temperature differences and heat fluxes

while introducing reduced calculation time. Process parameters may then be estimated according to geometry to ensure products of a particular quality (microstructure, residual stress, etc.) are produced.

### **Thermal Resistance Network Configuration**

#### *Model Development*

The schematic of the laser-based/blown-powder DED, or LENS, process, is shown in Figure 1 where a laser is directed at the center of the top layer of a deposited thin wall. Powder is fed into the melt pool created by the laser to form a weld bead in this model. During the actual DED process, the laser moves relative to the substrate in order to deposit a track of molten material rather than a bead. To simplify the problem, a static laser spot is studied at the center of deposited thin walls, which may represent a part's geometry at an arbitrary time during the build, to determine the effects of a varied geometry on average melt pool temperature and average temperature distribution within the part. Assumptions and idealizations employed for the model follow many of those discussed by Pinkerton & Li [20] and are omitted for brevity. Additional assumptions include:

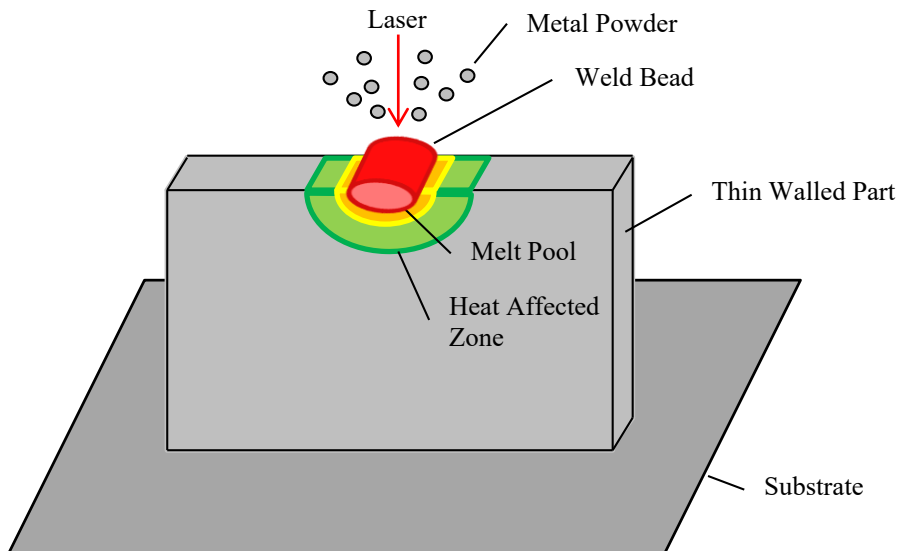


**Figure 1. Schematic of DED system in consideration.**

1. The laser is not moving along part, and no preheat exists on the part's surface.
2. The initial condition consists of the melt pool. That is, some volume of material is assumed to have already experienced a phase change to a liquidus state. This is a valid assumption since the tested processing variables is known to create parts through experimentation.
3. Rosenthal's closed-form solution [12] to the heat equation of a moving point heat source on an infinitely large substrate may be used to find the depth of the melt pool.
4. Only the melt pool surface area is radiating to the environment.
5. Surrounding environment is an enclosed volume at room temperature significantly larger than the part being fabricated.

6. The thin wall is sufficiently tall such that its temperature at the bottom is in thermal equilibrium with surroundings.
7. The empirical correlation for the convection heat transfer coefficient in vicinity of the melt pool as devised by Heigel et al. [21] is valid.
8. Single phase heat transfer within the melt pool may be modeled using an effective thermal conductivity as described by Lindgren [22].
9. The part behaves as a fin during laser irradiation; i.e., one dimensional, hyperbolic conduction.

The heat transfer initiating from the surface of the melt pool, originating from the incident laser, is determined by compensating for thermal exchange with the injected powder cloud and spectral limitations of interacting media. Pinkerton and Li's model is employed here by making similar assumptions [20]. Laser power absorbed and reflected by particles within an inner region to the melt pool is given by Eqs. (1) - (2), respectively [20]. The blown-powder, laser-based DED of titanium alloy, Ti-6Al-4V, is chosen as the modeled scenario. The material properties and process parameter values used for calculations are given in Table 1 and Table 2, respectively, along with the symbols for each.

$$q_{ap1} = \frac{3\zeta_{p,Ti}\dot{m}D_1l_b}{\pi r_{powder}v_{powder}\rho_s D_0^3} \cdot q_{input} \quad (1)$$

$$q_{rp1} = \frac{3(1 - \zeta_{p,Ti})\dot{m}D_1l_b}{\pi r_{powder}v_{powder}\rho_s D_0^3} \cdot q_{input} \quad (2)$$

The solid absorption,  $\zeta_{p,Ti}$ , is dependent upon laser type and has here been idealized at 1.064  $\mu\text{m}$  (wavelength of common Nd:YAG lasers) and 473 K to take into account an expected heating of the powder. Power absorbed and reflected within an outer region to the melt pool is given by Eqs. (3) - (4), respectively.

$$q_{ap2} = \frac{3\zeta_{p,Ti}\dot{m}(D_0 - D_1)l_b}{\pi r_{powder}v_{powder}\rho_s D_0^3} \cdot q_{input} \quad (3)$$

$$q_{rp2} = \frac{3(1 - \zeta_{p,Ti})\dot{m}(D_0 - D_1)L_b}{\pi r_{powder}v_{powder}\rho_s D_0^3} \cdot q_{input} \quad (4)$$

These output values are then combined to create a compensated power input (W) per Pinkerton et al. [20],  $q_I$ , by using Eq. (5).

$$q_I = \zeta_{p,Ti}(q_{input} - q_{ap1} - q_{ap2} - q_{rp1} - q_{rp2}) + q_{ap1} \quad (5)$$

The compensated power is then used as the input energy in Rosenthal's moving heat source equation, since it considers particle interactions before the laser powder is incident to the melt pool. Rosenthal is used to determine the depth of the melt pool,  $d_{mp}$ , so that the melt pool may be modeled in the system as an oblate, ellipsoidal component whose diameter is determined by the laser beam,  $D_1$ , and whose deposited height is equal to the depth.

**Table 1. Material properties used for model (all for Ti-6Al-4V unless otherwise noted).**

<b>Material Property (Symbol)</b>	<b>Value</b>
Melt temperature ( $T_{\text{melt}}$ )	1933 K [23]
Density of solid ( $\rho_s$ )	4.42 g/cm <sup>3</sup> [23]
Average density of liquid ( $\rho_l$ )	4.122 g/cm <sup>3</sup> [24]
Latent heat of fusion ( $L$ )	290 J/g [25]
Specific heat capacity of liquid ( $c_{p,l}$ )	760 J/kg·K [26], [27]
Specific heat capacity of solid ( $c_{p,s}$ )	610 J/kg·K [27]
Thermal conductivity of solid ( $k_s$ )	21 W/m·K [27]
Effective thermal conductivity of melt pool ( $k_{\text{mp}}$ )	100 W/m·K [22], [28]
Liquid emissivity ( $\epsilon_l$ )	0.4 [29]
Solid reflectivity of Titanium ( $\lambda_{\text{Ti}}$ ) @ 1.064 μm and 473 K	0.35 [30]
Solid absorption of Titanium ( $\zeta_{p,\text{Ti}}$ ) @ 1.064 μm and 473 K	0.65
Thermal diffusivity ( $\alpha_s$ )	7.79 mm <sup>2</sup> /s
<b>Equipment Properties (Symbol)</b>	
Initial laser beam and powder stream diameters ( $D_0$ )	10 mm
Diameter of laser beam and melt pool ( $D_1$ )	1.6 mm
Beam-powder interaction distance ( $l_b$ )	8.45 mm
Ambient temperature ( $T_\infty$ )	303.15 K
<b>Powder Stream Properties (Symbol)</b>	
Powder stream velocity ( $v_{\text{powder}}$ )	1.462 m/s
Powder particle radius ( $r_{\text{powder}}$ )	96.5 μm

**Table 2. DED process parameters used for model and experimentation.**

<b>Process Parameter</b>	<b>Laser Power (<math>q_{\text{input}}</math>)</b>	<b>Scan Speed (<math>v_{\text{laser}}</math>)</b>	<b>Powder Feed Rate (<math>\dot{m}</math>)</b>
<b>Value</b>	300 W	12.7 mm/s	0.32 g/s

Laser power is further compensated by subtracting energy absorbed by the melt pool's latent heat of fusion; assuming that the melt pool is already liquidus as the initial condition. The overall process is modeled as a non-moving laser; however, energy lost to latent heating is a known function of relative laser scan speed. For instance, more energy would be lost to latent heating if the scan speed were increased, because less power would be supplied to an area due to small surface-laser interaction times. This lost power contributes toward keeping the melt pool in a liquid state. In order to devise a relationship between latent heat of fusion and lost power, the melt pool is represented as an ellipse perpendicular to the scan path moving at some velocity as shown in Figure 3. The following equation for lost power to latent heating is then determined:

$$q_{\text{melt}} = L \cdot \rho_s \cdot 2 \cdot d_{\text{mp}} \cdot D_1 \cdot v_{\text{laser}} \quad (6)$$

Equation (6) describes the power required to maintain moving, molten metal mass described by the cross-sectional area of the melt pool shown in Figure 3. The value of Eq. (6) is then subtracted from the net heat flux inputted to yield a final, adjusted value for power input into the thermal circuit,  $q_{\text{II}}$ .

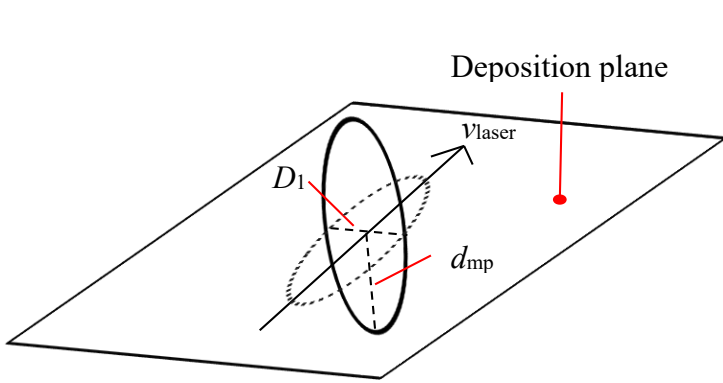


**Figure 3. Depiction of melt pool as it moves along a plane of deposition.**

#### Thermal Resistance Model

The thermal resistance model considers the temperature response of a completed thin wall that has had time to cool to room temperature and is subjected to heating in the center of the top edge. The latent/spectral/powder compensated, DED heat transfer through the melt pool and part, as well as with the environment, is modeled using a procedure similar to Figure 2 and a thermal resistance network shown in Figure 4. Ohm's analogy likens the heat flow to electrical current through a circuit and temperature difference to voltage difference at nodes. Resistors represent an item that restricts the heat flow and can arise due to conduction, thermal spreading, contact area, etc. A material may also store heat energy in the same way a capacitor in an electrical circuit stores energy. The amount of heat flow through a resistor,  $q_{\text{resist}}$ , and capacitor,  $q_{\text{cap}}$ , is given by Eqs. (7) & (8), respectively.

$$q_{\text{resist}} = \frac{\Delta T}{R} \quad (7)$$

$$q_{\text{cap}} = C \frac{dT}{dt} \quad (8)$$

where  $R$  represents any resistance,  $\Delta T$  is the temperature difference between nodes on either side of a resistance,  $C$  is a material's capacitance as

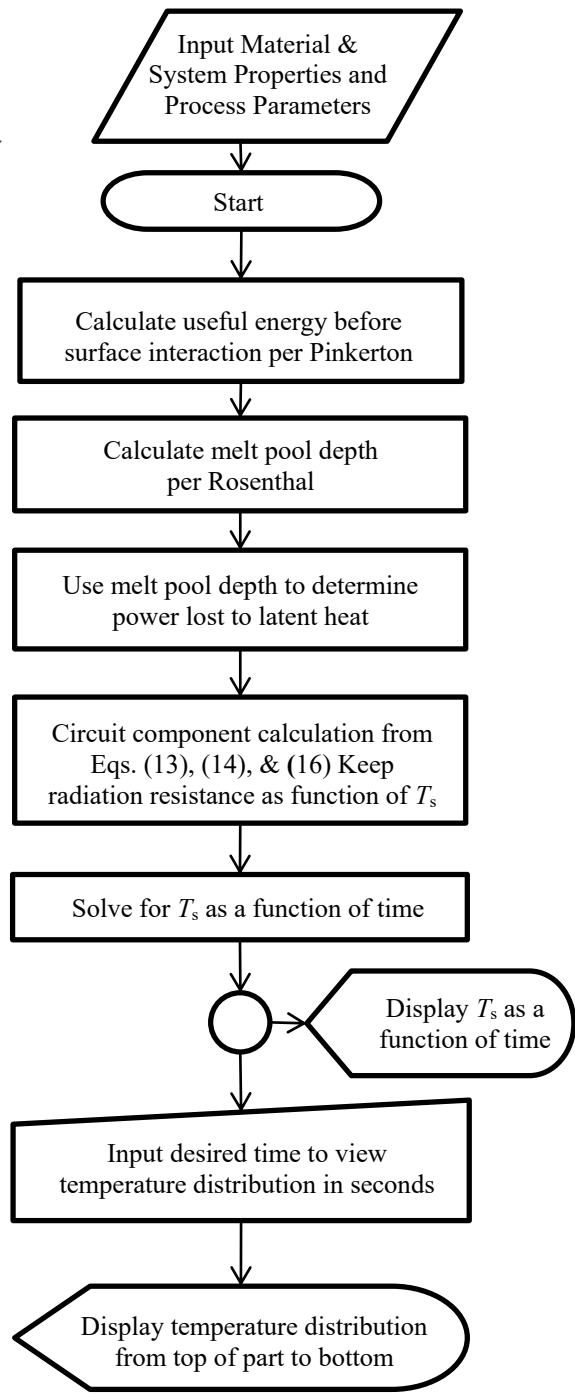


**Figure 2. Process chart to determine the temperature distribution within a part.**

determined by Eq. (14), and  $dT/dt$  is a temperature difference overtime as experienced by the capacitor. A positive  $dT/dt$  indicates that the capacitor is being charged, whereas a negative value indicates that the capacitor is being discharged.

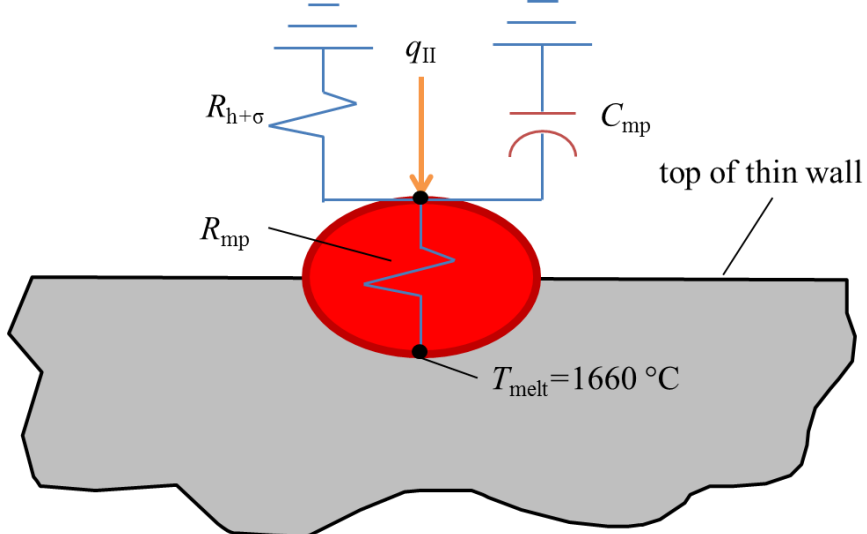


**Figure 4. Thermal resistance network representation of heat transfer during the DED of a rectangular wall**

The empirical, forced convection model developed by Heigel et al. [21] is employed to calculate a heat transfer coefficient across a thin wall,  $h_{\text{wall}}$ . The correlation is given below:

$$h_{\text{wall}} = (-2.717z + 37.174) \cdot e^{-(0.107r)^{2.7}} + h_{0\text{wall}} \quad (9)$$

where  $z$  is the distance from the powder supply nozzles to the top of the wall in mm,  $r$  is the distance from the jet centerline to a point of interest in mm, and  $h_{0\text{wall}}$  is the free-convection coefficient near  $25 \text{ W/m}^2\text{-K}$  [21]. Free convection becomes dominant around  $r = 15 \text{ mm}$ . In the overview schematic of Figure 4, this resistance is only connected to the surface temperature of the melt pool; hence, Eq. (9) is only integrated over  $r$  as the diameter of the melt pool. The value for  $z$  is held constant at  $l_b$  as defined in Table 1.

The temperature-dependent, radiation heat transfer coefficient,  $h_\sigma(T_s)$ , is described in Eq. (10):

$$h_\sigma(T_s) = \varepsilon_l \sigma (T_s + T_\infty)(T_s^2 + T_\infty^2) \quad (10)$$

where  $\sigma$  is the Stefan-Boltzmann constant,  $5.67 \cdot 10^{-8} \text{ W/m}^2\text{-K}^4$ . The heat transfer coefficients are then converted into thermal resistance via Ohm's analogy and the following equations result:

$$R_h = 1/h_{\text{wall}} A_{\text{mp}} \quad (11)$$

$$R_\sigma = 1/h_{\text{rad}}(T_s) A_{\text{mp}} \quad (12)$$

where  $A_{mp}$  is the surface area of the oblate, ellipsoidal melt pool with two diameters equal to  $D_l$  and the other equal to twice the  $d_{mp}$ . The resistances are then combined in parallel to yield  $R_{h+\sigma}$  by:

$$R_{h+\sigma}^{-1} = R_h^{-1} + R_\sigma^{-1} \quad (13)$$

The capacitance of the melt pool,  $C_{mp}$ , is dependent upon amount and properties of the melted material and is defined in Eq. (14):

$$C_{mp} = c_{p,l}\rho_l V_{mp} \quad (14)$$

where  $V_{mp}$  is the volume of the melt pool. The melt pool is assigned an effective thermal conductivity,  $k_{mp}$ ; therefore, the resistance through the melt pool,  $R_{mp}$ , is calculated using a standard conductive resistance model:

$$R_{mp} = d_{mp} / k_{mp} A_{mp} \quad (15)$$

In the thermal circuit shown Figure 4, the top node receives the compensated heat transfer input from the laser and represents the melt pool surface temperature. From this node, heat (analogous to current in an electrical circuit) is allowed to flow to the convective/radiative resistance ( $R_h + R_\sigma$ ), melt pool capacitance ( $C_{mp}$ ), and melt pool ( $R_{mp}$ ). The addition of the three heat flows should add to give  $q_{II}$ . Convective, radiative, and capacitive resistances were all modeled as to terminate at ambient temperature. For the capacitor, the environment determines the amount of energy storage available. The same amount of power going into the combined melt pool and spreading resistances will also travel through the bulk part. However, average temperature (analogous to voltage in an electrical circuit) of the melt pool surface,  $T_s$ , and melt pool bottom,  $T_{melt}$ , will be dissimilar. The former value will be unknown while the latter is the material's liquidus temperature. By knowing the input power, ambient temperature, and temperature at the bottom of the melt pool, the average surface temperature of the melt pool may be found. Only an average temperature is found due to the one-dimensional nature of the system.

Finally, the intra-part heat transfer after the melt pool was assumed to be representative of heat transfer from an extended surface. The hyperbolic equation used to describe the temperature distribution within a rectangular fin of prescribed end temperature is used. The equation has been excluded for brevity, but is well known and easily accessed [31]. Since the current setup is essentially a “reversed fin”, the “base temperature” (hot side) of the fin is taken as the average temperature of the upper surface. This distribution is solved while accounting for the convection around the part as well as the conduction through it. Rosenthal’s solution has been utilized to determine the average temperature of the part’s upper surface between the edges of the part and melt pool. The value is used as the upper surface temperature in the fin temperature distribution. Average melt pool temperature is calculated directly from the resistance network and is included in the overall surface average.

## Experiments

The two thin walls of different lengths in Figure 5 were printed in order to validate the current model. Because the walls were thin, no value was prescribed for the wall thickness which was measured to be around 2 mm after fabrication. This thickness is largely a result of the selected process parameters used in Table 2 which were determined before hand through experimentation to yield fully dense thin walls. Height was kept constant at 21.09 mm and length,  $a$ , was changed from 25.4 mm to 50.8 mm. An OPTOMECH LENS™ 750 system with a Nd:YAG laser was used, in conjunction with spherical Ti-6Al-4V particles. The molten metal was deposited track upon track to build up the thin walls atop a substrate of the same material by moving a build platform underneath the static laser.

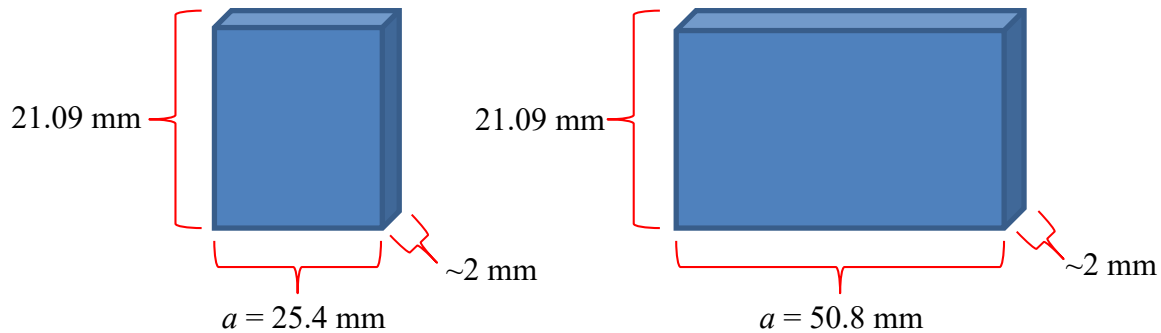


**Figure 5. Dimensions of thin walls used in experiments to validate model.**

An infrared (IR) camera (calibrated to black-body temperature) mounted to the moving build platform gathered images of the bulk thermal histories of each wall. The IR camera possessed a spectral response range of 8–14  $\mu\text{m}$  and was set to capture images at a rate of 14 Hz. Each pixel was found to correspond roughly to about 0.37 mm on the build. Because IR cameras are difficult to calibrate to true temperatures due to a materials emissivity's dependence on view angle and spectrum, normalized IR values were used in model comparisons. To do this, each row of pixels extending from edge to edge along the length,  $a$ , of the wall was averaged together from the top of the wall to the bottom. An average temperature distribution along the height of the walls was thus obtained. The distribution was then normalized by dividing all of the average values by the maximum average value. Each image at the temporal mid-point and end of the build was processed individually in the same fashion with the laser at the center of the upper surface.

A dual-wavelength (DW) pyrometer was set up to view the melt pool at all times and captured images at a rate between 4 – 7 Hz. For each image, all temperature values exceeding  $T_{\text{melt}}$  were averaged together to determine the experimental, average melt pool temperature. Melt pool images and the immediate heat affected zone (HAZ) are shown in Figure 6 (a) and (b) during the final layer of the small and long length builds, respectively. Any values greater than  $T_{\text{melt}}$  belong to the melt pool while the rest are part of the HAZ (values < 1300 °C are considered noise

and have been excluded). The melt pools are shown to be of relatively the same size and shape, though (b) shows slightly higher average temperature values.

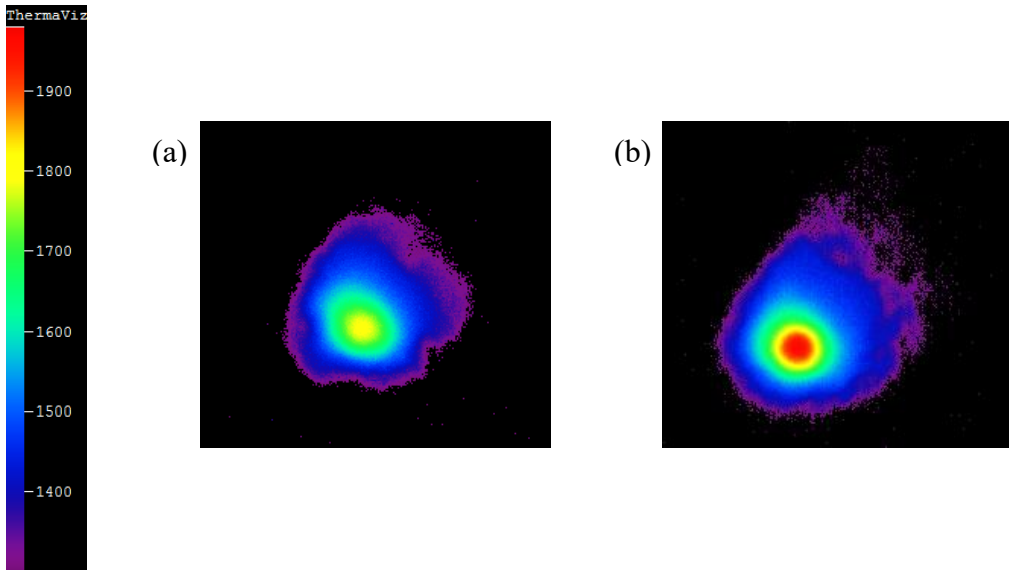


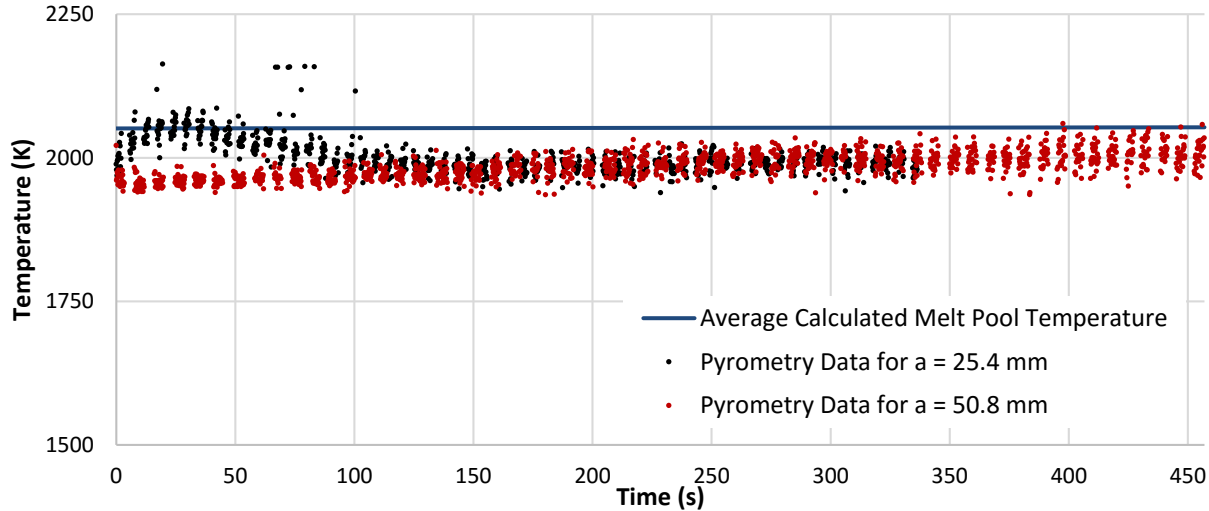
**Figure 6. Melt pool images taken as the laser deposited in the center of the part during the final layer of the  $a = 25.4$  mm (a) and  $a = 50.8$  mm (b) builds.  
Temperature scale in °C.**

### Results & Discussion

The calculated, average melt pool temperature using the thermal resistance network and experimentally-measured, average melt pool temperature from the two thin wall builds are shown together in Figure 7. As calculated, the average melt pool temperature was found to be 2051 K for both sized walls. In fact, the height of the wall was not found to affect this value within the ranges tested. The calculated value translates to an error of 2% and 3% for the 25.4 mm and 50.8 mm tall walls respectively. Pyrometry data agree with the calculations to the extent that the highest sustained temperature of the melt pool is the same. One should recall that the calculations from the thermal network occurred with a still laser whose temperature was found to reach steady state around 2 s after being turned on. The experiment itself consisted of consecutive layers building upon each other, and the data it produced shows average melt pool temperature at every point during the build. Figure 7 shows that the wall of smaller  $a$  value starts at a certain temperature, steadily rises, and then achieves steady-state temperature similar in magnitude to which it began.

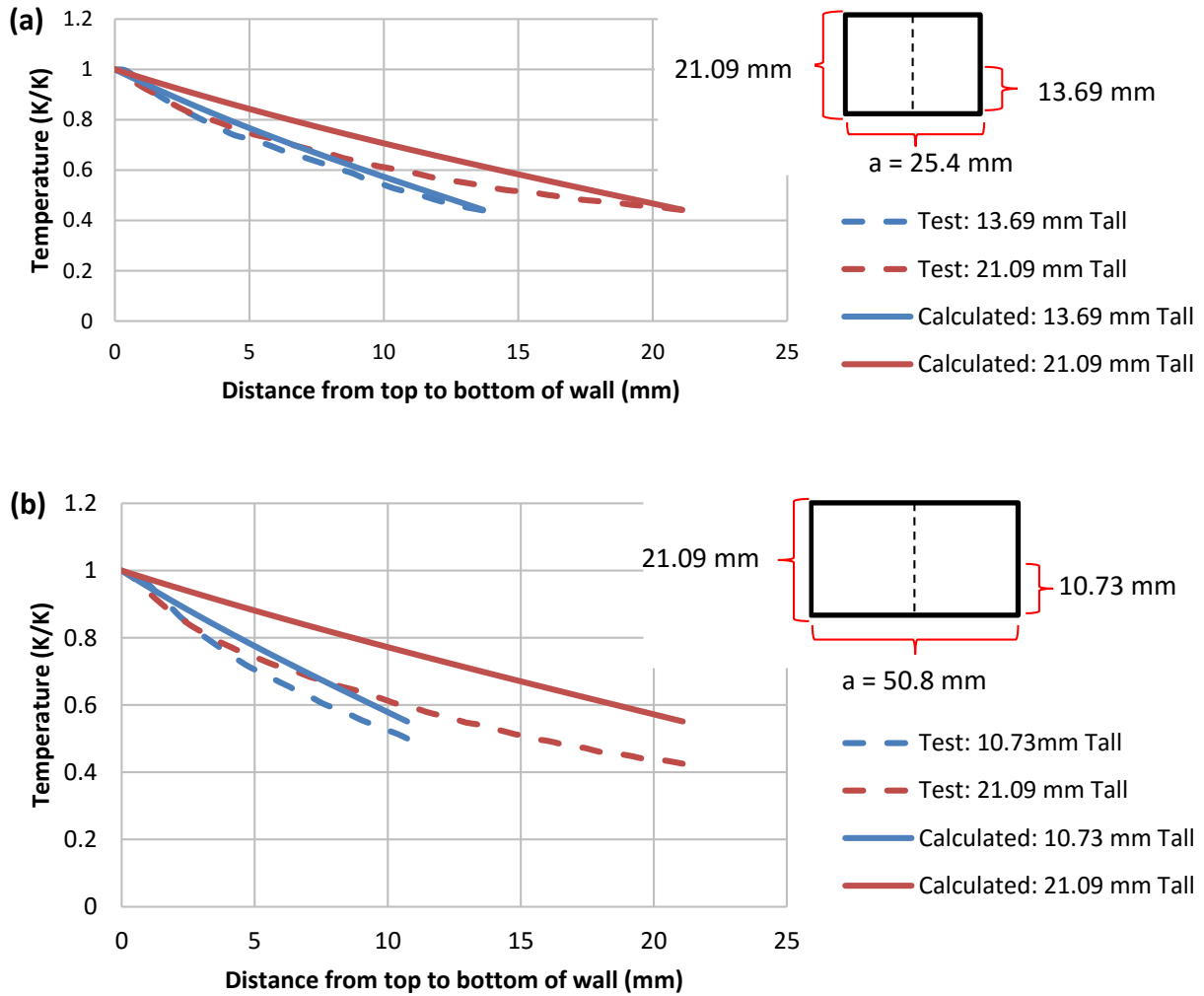
Bulk temperature data was gathered by an in-chamber, infrared (IR) camera mounted on the moving stage to which the substrate was secured. The average temperature distribution was extracted from the top to the bottom of each thin wall geometry at the temporal mid-point of the build as well as the completion. Part temperature distribution was modeled as a fin with prescribed values for end temperatures as mentioned in the previous section. The results of this model represent the average temperature distribution along the height of the part. To normalize these values, the points on the temperature distribution were divided by the maximum, calculated value.

Comparative results between normalized experimental and model data are shown in Figure 8 (a) and (b).



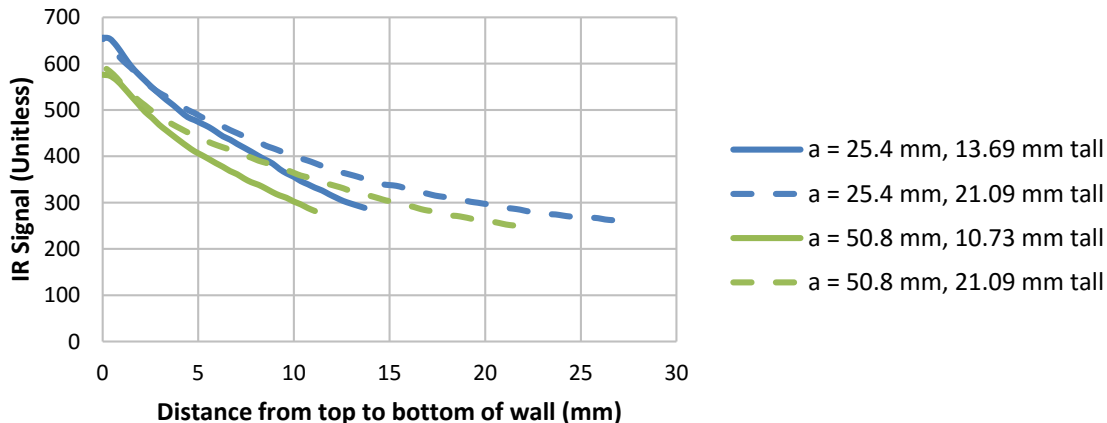
**Figure 7. Comparison of average melt pool temperature between the  $a = 25.4\text{mm}$  and  $a = 50.8\text{mm}$  thin walls against build time. Each pyrometry data point shows the average temperature of the melt pool at a given time. The calculated, average temperature was found via the resistance network.**

Figure 8 (a) shows the normalized, average temperature distribution along the thin wall of smaller length. As seen in the figure, values align at the top and bottom of the wall at both wall heights. This is, of course, expected since the top of the wall is being heated while the bottom is near ambient conditions. However, the modeled distribution predicts a linear decay as opposed to the exponential decay shown by the data. This suggests that the free convection, heat transfer coefficient used in the fin model is too low. Upon increasing this coefficient, the model begins to approach the experimental data. When the length of the part is increased, the model seems to decrease in accuracy. While an increased heat transfer coefficient will still cause the model to approach the data, the normalized endpoints remain incongruent. This phenomenon may be related more to the experimental conditions than the modeled conditions. Depending on the relative location of the part to the IR camera, results could vary slightly due to the angular variance of a material's emissivity.



**Figure 8. Test and calculation comparisons of  $a=25.4$  mm (a) and  $a = 50.8$  mm (b) thin wall temperature profile.**

Finally, the uncalibrated, bulk, average temperature distributions from the experimental IR data are compared in Figure 9. Higher surface temperature is seen in the smaller length thin walls than the larger – a trend that is mimicked by the fin-modeled distribution. This occurrence may not only be explained by the smaller dwell time between layers for the smaller build, but it may also be attributed to the edge-effects in the build. Since the part is smaller, more heat tends to remain near the edges: increasing average temperature. Furthermore, the longer build shows a lower relative temperature simply because there is a greater length of the build. Thus, the expanse of the lower temperatures is greater from edge to edge. Because of these observations, average temperature distribution within the part is shown to be dependent upon size. This conclusion has little merit in-and-of itself, but it does suggest that thermal gradients within the part will be different as size changes. Grain growth would then be indirectly affected through the average temperature distribution.



**Figure 9. Comparison between the average temperature distribution of the thin walls of varying lengths shown near halfway (solid lines) and at the completion (dashed lines) of the builds. The IR signal has not been calibrated and is therefore considered unitless.**

### Conclusions

A thermal resistance network to determine the average surface temperature of the melt pool has been devised and validated against experimental data. The calculated surface temperature is in good agreement with the data, and does not appear to vary with increased wall length. However, further experiments are hypothesized to show a decreased average melt pool temperature with increased thickness. The model may aid in selecting preliminary parameters (particularly laser power and powder feed rate) to aim for a certain average melt pool temperature. This can be useful when minimizing energy input is desired.

Average temperature along the height of the thin wall has also been idealized as a fin temperature distribution with Dirichlet boundary conditions. When compared to normalized, experimental data the idealized results seem to suggest that a higher heat transfer coefficient in the model would be required to approach the real-life trend. Average temperature distribution within the wall was shown to decrease with increased thin wall length by both model and data values. Though this does not directly correspond to a change in microstructure, it may suggest a change in thermal gradients that could affect grain growth direction.

Model results may be improved by incorporating thermal resistances into the model. Better understanding on the connection between thermal spreading and the melt pool will be explored in order to increase accuracy of the melt pool temperature prediction. Future research will also aim to solve the heat equation for thermal spreading with DED boundary conditions as well as a moving heat source. Such an equation will allow researchers to further understand the part's size effect on melt pool and bulk temperature distributions.

The thermal network presented is a step towards creating a tool that may be used by researchers as a preliminary to parameter selection when part size is changed. It is not meant to replace detailed FEA models, but is intended to service those who may not have access to large, data-handling hardware or FEA software. This model is also not meant to replace process maps that present relationships between process parameters (laser power, scan speed, etc.) and part

properties (solidification microstructure, residual stresses, etc.). However, it aims to supplement these maps by providing thermal information on detailed geometries.

### **Acknowledgements**

Research was partially sponsored by the Army Research Laboratory and was accomplished under Cooperative Agreement Number W911NF-15-2-0025. The views and conclusions contained in this document are those of the authors and should not be interpreted as representing the official policies, either expressed or implied, of the Army Research Laboratory or the U.S. Government. The U.S. Government is authorized to reproduce and distribute reprints for Government purposes notwithstanding any copyright notation herein. This manuscript was prepared while Nima Shamsaei, Scott Thompson and Steve R. Daniewicz were faculty at Mississippi State University.

### **References**

- [1] M. L. Griffith, D. M. Keicher, C. L. Atwood, J. A. Romero, J. E. Smugeresky, L. D. Harwell, and D. L. Greene, "Free Form Fabrication of Metallic Components Using Laser Engineered Net Shaping (LENS)," in *Proceedings of the 7th Solid Freeform Fabrication Symposium*, 1995, pp. 125–132.
- [2] M. L. Griffith, M. E. Schlienger, L. D. Harwell, M. S. Oliver, M. D. Baldwin, M. T. Ensz, M. Essien, J. Brooks, C. V Robino, J. E. Smugeresky, W. H. Hofmeister, M. J. Wert, and D. V Nelson, "Understanding Thermal Behavior in the LENS Process," *Mater. Des.*, vol. 20, no. 2–3, pp. 107–113, 1999.
- [3] S. Bontha and N. W. Klingbeil, "Thermal Process Maps for Controlling Microstructure in Laser-Based Solid Freeform Fabrication," in *Solid Freeform Fabrication Symposium*, 2003, pp. 219–226.
- [4] A. R. Nassar, J. S. Keist, E. W. Reutzel, and T. J. Spurgeon, "Intra-Layer Closed-Loop Control of Build Plan during Directed Energy Additive Manufacturing of Ti–6Al–4V," *Addit. Manuf.*, vol. 6, pp. 39–52, Apr. 2015.
- [5] C. Qiu, G. A. Ravi, and M. M. Attallah, "Microstructural Control during Direct Laser Deposition of a b -Titanium Alloy," *J. Mater. Des.*, vol. 81, pp. 21–30, 2015.
- [6] A. J. Sterling, B. Torries, N. Shamsaei, S. M. Thompson, and D. W. Seely, "Fatigue Behavior and Failure Mechanisms of Direct Laser Deposited Ti – 6Al – 4V," *Mater. Sci. Eng. A*, vol. 655, pp. 100–112, 2016.
- [7] J. Yu, M. Rombouts, G. Maes, and F. Motmans, "Material Properties of Ti6Al4V Parts Produced by Laser Metal Deposition," vol. 39, pp. 416–424, 2012.
- [8] M. L. Griffith, M. T. Ensz, J. D. Puskar, C. V Robino, J. A. Brooks, J. Philliber, J. E. Smugeresky, and W. H. Hofmeister, "Understanding the Microstructure and Properties of Components Fabricated by Laser Engineered Net Shaping (LENS)," in *Materials Research Society Proceedings*, 2000.
- [9] B. E. Carroll, A. Palmer, and A. M. Beese, "Anisotropic Tensile Behavior of Ti – 6Al – 4V Components Fabricated with Directed Energy Deposition Additive Manufacturing," *Acta Mater.*, vol. 87, pp. 309–320, 2015.
- [10] W. Liu and J. N. DuPont, "Fabrication of Functionally Graded TiC/Ti Composites by Laser Engineered Net Shaping," *Scr. Mater.*, vol. 48, pp. 1337–1342, 2003.
- [11] A. Bandyopadhyay, B. V. Krishna, W. Xue, and S. Bose, "Application of Laser Engineered Net Shaping (LENS) to Manufacture Porous and Functionally Graded Structures for Load Bearing Implants," *J. Mater. Sci. Mater. Med.*, vol. 20, pp. S29–S34, 2009.
- [12] D. Rosenthal, "The Theory of Moving Sources of Heat and Its Application to Metal Treatments," *Trans. Am. Soc. Mech. Eng.*, vol. 68, pp. 849–866, 1946.
- [13] A. Vasinonta and J. Beuth, "Process Maps for Laser Deposition of Thin-Walled Structures," in *Solid Freeform Fabrication Symposium*, 1999, pp. 383–392.

- [14] J. Beuth and N. Klingbeil, “The Role of Process Variables in Laser-Based Direct Metal Solid Freeform Fabrication,” *JOM*, vol. 53, no. 9, pp. 36–39, 2001.
- [15] A. C. Nunes, “An Extended Rosenthal Weld Model,” *Weld. J.*, p. 165s–170s, 1983.
- [16] N. W. Klingbeil, S. Bontha, C. J. Brown, and D. R. Gaddam, “Effects of Process Variables and Size Scale on Solidification Microstructure in Laser-Based Solid Freeform Fabrication of Ti-6Al-4V,” in *Solid Freeform Fabrication Symposium*, 2004, pp. 92–103.
- [17] J. Gockel, N. Klingbeil, and S. Bontha, “A Closed-Form Solution for the Effect of Free Edges on Melt Pool Geometry and Solidification Microstructure in Additive Manufacturing of Thin-Wall Geometries,” *Metall. Mater. Trans. B*, vol. 47, no. 2, pp. 1400–1408.
- [18] N. Ondrej, V. Ocelík, A. Palavra, and J. T. M. Hosson, “The Prediction of Coating Geometry from Main Processing Parameters in Laser Cladding,” *Phys. Procedia*, vol. 56, pp. 220–227, 2014.
- [19] A. J. Pinkerton, “An Analytical Model of Beam Attenuation and Powder Heating during Coaxial Laser Direct Metal Deposition,” *J. Phys. D. Appl. Phys.*, vol. 40, pp. 7323–7334, 2007.
- [20] A. J. Pinkerton and L. Li, “An Analytical Model of Energy Distribution in Laser Direct Metal Deposition,” in *Proceedings of the Institution of Mechanical Engineers, Part B: Journal of Engineering Manufacture*, 2004, vol. 218, pp. 363–374.
- [21] J. C. Heigel, P. Michaleris, and E. W. Reutzel, “Thermo-Mechanical Model Development and Validation of Directed Energy Deposition Additive Manufacturing of Ti – 6Al – 4V,” *Addit. Manuf.*, vol. 5, pp. 9–19, 2015.
- [22] L. Lindgren, “Finite Element Modeling and Simulation of Welding, Part 2: Improved Material Modeling,” *J. Therm. Stress.*, vol. 24, pp. 195–231, 2001.
- [23] Timet, “TIMET 6-4 Titanium Alloy (Ti-6Al-4V; ASTM Grade 5) Rod,” 2015. [Online]. Available: <http://www.matweb.com/search/DataSheet.aspx?MatGUID=f0d81a62a0564398b1b17e851841e0c4&ckck=1>. [Accessed: 23-Jun-2016].
- [24] J. J. Z. Li, W. L. Johnson, and W. K. Rhim, “Thermal Expansion of Liquid Ti-6Al-4V Measured by Electrostatic Levitation,” *Appl. Phys. Lett.*, vol. 89, no. 11, pp. 80–82, 2006.
- [25] M. J. Torkamany, F. Malek Ghaini, and R. Poursalehi, “An Insight to the Mechanism of Weld Penetration in Dissimilar Pulsed Laser Welding of Niobium and Ti-6Al-4V,” *Opt. Laser Technol.*, vol. 79, pp. 100–107, 2016.
- [26] D. Basak, R. a. Overfelt, and D. Wang, “Measurement of Specific Heat Capacity and Electrical Resistivity of Industrial Alloys using Pulse Heating Techniques,” *Int. J. Thermophys.*, vol. 24, no. 6, pp. 1721–1733, 2003.
- [27] R. Rai, J. W. Elmer, T. a Palmer, and T. DebRoy, “Heat Transfer and Fluid Flow during Keyhole Mode Laser Welding of Tantalum, Ti-6Al-4V, 304L Stainless Steel and Vanadium,” *J. Phys. D. Appl. Phys.*, vol. 40, no. 18, pp. 5753–5766, 2007.
- [28] M. P. Mughal, H. Fawad, and R. Mufti, “Finite Element Prediction of Thermal Stresses and Deformations in Layered Manufacturing of Metallic Parts,” *Acta Mech.*, vol. 183, no. 1–2, pp. 61–79, 2006.
- [29] M. Boivineau, C. Cagran, D. Doytier, V. Eyraud, M. H. Nadal, B. Wilthan, and G. Pottlacher, “Thermophysical Properties of Solid and Liquid Ti-6Al-4V (TA6V) Alloy,” *Int. J. Thermophys.*, vol. 27, no. 2, pp. 507–529, 2006.
- [30] E. W. Spisz, A. J. Weigund, R. L. Bowman, and J. R. Juck, “Solar Absorptances and Spectral Reflectances of 12 Metals for Temperatures Ranging From 300 To 500 K,” Washington, D.C., 1969.
- [31] F. P. Incropera, D. P. Dewitt, T. L. Bergman, and A. S. Lavine, *Fundamentals of Heat and Mass Transfer*, Sixth Edit. Danvers, MA: John Wiley & Sons, 2007.